The Synthesis and Characterization of Sol-Gel-Derived SrTiO₃-BiMnO₃ Solid Solutions

Dovydas Karoblis [1], Ramunas Diliautas [1], Eva Raudonyte-Svirbutaviciene [2], Kestutis Mazeika [3], Dalis Baltrunas [3], Aldona Beganskiene [1], Aleksej Zarkov [1,*] and Aivaras Kareiva [1]

[1] Institute of Chemistry, Vilnius University, Naugarduko 24, LT-03225 Vilnius, Lithuania; dovydas.karoblis@chgf.vu.lt (D.K.); ramunas.diliautas@bioeksma.lt (R.D.); aldona.beganskiene@chf.vu.lt (A.B.); aivaras.kareiva@chgf.vu.lt (A.K.)

[2] SRI Nature Research Centre, Institute of Geology and Geography, Akademijos 2, LT-08412 Vilnius, Lithuania; eva.svirbutaviciene@gamtc.lt

[3] Center for Physical Sciences and Technology, LT-02300 Vilnius, Lithuania; kestas@ar.fi.lt (K.M.); dalis@ar.fi.lt (D.B.)

[*] Correspondence: aleksej.zarkov@chf.vu.lt

Abstract: In this study, the aqueous sol-gel method was employed for the synthesis of $(1-x)$SrTiO₃-xBiMnO₃ solid solutions. Powder X-ray diffraction analysis confirmed the formation of single-phase perovskites with a cubic structure up to $x = 0.3$. A further increase of the BiMnO₃ content led to the formation of a negligible amount of neighboring Mn₃O₄ impurity, along with the major perovskite phase. Infrared (FT-IR) analysis of the synthesized specimens showed gradual spectral change associated with the superposition effect of Mn-O and Ti-O bond lengths. By introducing BiMnO₃ into the SrTiO₃ crystal structure, the size of the grains increased drastically, which was confirmed by means of scanning electron microscopy. Magnetization studies revealed that all solid solutions containing the BiMnO₃ component can be characterized as paramagnetic materials. It was observed that magnetization values clearly correlate with the chemical composition of powders, and the gradual increase of the BiMnO₃ content resulted in noticeably higher magnetization values.

1. Introduction

Multiferroics are considered a multifunctional class of compounds, in which at least two ferroic orders (ferroelastic, ferromagnetic, or ferroelectric) exist simultaneously. In this type of material, the manipulation of magnetic properties is possible via the application of an external electric field and controllability of ferroic features can be achieved via the application of an external magnetic field [1,2]. The strong magnetoelectric coupling makes multiferroics useful in different kinds of technological fields, including gyrators [3], magnetic sensors [4], memory devices [5], etc. All multiferroic ceramics can be divided into two main groups: Single-phase compounds and composites. By combining phases responsible for ferroelectric and magnetic properties separately, the electrical, magnetic, and magnetoelectric characteristics can be improved in comparison with single-phase materials [6,7].

One of the most studied single-phase multiferroics is BiMnO₃ (BMO) [8]. In the form of a thin film, this material has shown good ferroelectric properties, with remnant polarization of 23 μC/cm² at 5 K [9] and 16 μC/cm² at room temperature [10]. Moreover, BMO is ferromagnetic at low temperatures in bulk (T_C = 105 K) [11] and thin film forms [12]. This perovskite-type material is considered metastable since heating at ambient pressure leads to its decomposition and the formation of Bi₂Mn₄O₁₀ and Bi₁₂MnO₂₀ phases [13]. Furthermore, for the preparation of BMO, a high pressure is

required [13,14], but even with the applied pressure, the formation of monophasic perovskite phase remains a challenging task.

$SrTiO_3$ (STO) is a well-known perovskite-type material, which can be applied in different technological fields, such as thermoelectrics [15], photocatalysis for water splitting [16], piezoelectrics [17], superconductors [18], solid oxide fuel cells [19], etc. This material is considered to be quantum paraelectric, since the ferroelectric ordering in the lower tetragonal symmetry is suppressed by quantum fluctuations [20]. Transition to the ferroelectric phase in this compound can be induced by different methods, including ^{16}O substitution by an ^{18}O isotope [21], cation substitution [22], or the application of intense terahertz electric field excitation [23]. The hydrothermal method [24], polymerized complex method [25], solid-state reaction [26], spray-drying [27], and molten salt [28] are a few of the synthetic approaches that have been previously employed for the synthesis of STO.

To the best of our knowledge, there is only one article regarding powdered (1−x)STO-xBMO solid solutions investigating compositions in the range of 30–70 mol% BMO [29]. It was observed that solid solutions prepared by the solid-state reaction method and having 60 and 70 mol% of BMO exhibited high room-temperature dielectric loss. However, the authors did not show the XRD patterns of their synthesized compounds. Therefore, there is no evidence of the formation of single-phase solid solution in such a broad compositional range. Taking into account the hardly achievable stabilization of materials containing 70 mol% of BMO, those results do not seem reliable. Additionally, perovskite BMO thin films can be synthesized on STO substrates [30]. Furthermore, solid solutions containing both STO and multiferroic perovskite, such as $BiFeO_3$ [31], can be prepared. On the other hand, BMO can be partially stabilized in a solid solution form with $PbTiO_3$ [32] or $LaMnO_3$ [33]. To the best of our knowledge, there are no studies reporting on the application of the sol-gel synthesis of STO-BMO solid solutions.

In the present work, we developed an aqueous sol-gel synthetic approach to prepare (1−x)$SrTiO_3$-x$BiMnO_3$ ((1−x)STO-xBMO) solid solutions for the very first time. The maximal substitution level, structural, morphological, and magnetic properties were investigated for all synthesized materials.

2. Experiment

2.1. Synthesis

For the synthesis of (1−x)STO-xBMO solid solutions, strontium nitrate ($Sr(NO_3)_2$, ≥99.0%, Sigma-Aldrich, Darmstadt, Germany), titanium (IV) isopropoxide ($C_{12}H_{28}O_4Ti$, ≥97%, Sigma-Aldrich, Darmstadt, Germany), bismuth (III) nitrate pentahydrate ($Bi(NO_3)_3 \cdot 5H_2O$, 98%, Roth, Karlsruhe, Germany), and manganese (II) nitrate tetrahydrate ($Mn(NO_3)_2 \cdot 4H_2O$, 99.9%, Alfa Aesar, Kandel, Germany) were used as precursors. For the typical synthesis of 1 g of solid solution with a 0.9STO-0.1BMO composition, 6.418 g of citric acid monohydrate ($C_6H_8O_7 \cdot H_2O$, 99.9%, Chempur, Piekary Slaskie, Poland) was firstly dissolved in 20 mL of distilled water (the ratio between total metal ions and citric acid was 1:3). Then, 1.360 mL of titanium isopropoxide was added and the hot plate temperature was adjusted to 90 °C. After mixing, a clear and transparent solution was obtained. In the next stage, 0.128 g of $Mn(NO_3)_2 \cdot 4H_2O$ and 0.970 g of $Sr(NO_3)_2$ were added to the above solution. Prior to the addition of bismuth (III) nitrate (0.2471 g), the pH value of the reaction mixture was adjusted to 1 by adding nitric acid (HNO_3, 65%). This was done in order to avoid the formation of insoluble bismuth oxynitrate $BiONO_3$ precipitates. After that, 5.960 mL of ethylene glycol ($C_2H_6O_2$, Sigma-Aldrich, ≥99.5%) was added to the transparent solution (the ratio between total metal ions and ethylene glycol was 1:10) and the mixture was homogenized at 90 °C for 1.5 h. For the formation of precursor gel, the evaporation of water was performed at 150 °C. The obtained gel was dried for 12 h at 180 °C, and the resulting powder was ground in a mortar and annealed at 1000 °C for 5 h in air atmosphere with a heating rate of 5 °C/min. For the synthesis of solid solutions of other chemical compositions, the required amount of starting materials was recalculated according to the stoichiometry of the final product.

2.2. Characterization

Thermogravimetric and differential scanning calorimetry (TG-DSC) analysis using an STA 6000 Simultaneous Thermal Analyzer (Perkin Elmer, Waltham, MA, USA) was applied to investigate the thermal decomposition of precursor gels. A typical amount of 5–10 mg of dried sample was heated from 30 to 900 °C at a 10 °C/min heating rate in dry flowing air (20 mL/min). A MiniFlex II diffractometer (Rigaku, The Woodlands, TX, USA) working in Bragg–Brentano ($\Theta/2\Theta$) geometry was used for powder X-ray diffraction analysis (XRD). The data were obtained within a 2Θ range from 20 to 80°, with a scanning speed of 5°/min and a step width of 0.02°. Lattice parameters were refined by the Rietveld method using the FullProf suite. Infrared (FT-IR) spectra were obtained in the range of 4000–400 cm^{-1} employing an ALPHA ATR (Bruker, Billerica, Ma, USA) spectrometer. The morphological features of the synthesized products were examined with an SU-70 field-emission scanning electron microscope (FE-SEM, Hitachi, Tokyo, Japan). ImageJ software (LOCI, WI, USA) was used to estimate the particle size distribution from SEM images. For magnetic measurements, powdered sample (100 mg) was placed in a plastic straw with a 5 mm diameter with a sample height of approximately 5 mm and embedded between foam plugs. The dependence of the magnetization of samples on the strength of the magnetic field was recorded using a magnetometer consisting of an SR510 lock-in amplifier (Stanford Research Systems, Gainesville, GA, USA), an FH-54 Gauss/Teslameter (Magnet Physics, Cologne, Germany), and a laboratory magnet supplied by an SM 330-AR-22 power source (Delta Elektronika, Eindhoven, The Netherlands).

3. Results and Discussion

A thermogravimetric analysis of precursor gels of two different compositions was performed in order to determine the possible temperature of the formation of solid-solutions and to investigate the thermal decomposition behavior. TG-DTG-DSC curves of the gel corresponding to the final STO composition are depicted in Figure 1. It can be seen that thermal degradation of the Sr-Ti-O gel can be divided into three main steps. The first step can be associated with the loss of absorbed water, during which only an insignificant amount of the initial weight (2–3%) is lost. This process occurs in the range of approximately 100–150 °C. The second weight loss takes place at around 300 °C, and this step can be attributed to the decomposition of the organic framework of the gel. Finally, the last weight loss can be seen in the 450–500 °C temperature range. This step is accompanied by a strong exothermic peak, which is clearly seen from the DSC curve. The third stage can be ascribed to the combustion reaction between nitrates and residual organic parts of the gel. The residual mass remains constant at temperatures above 540 °C. The total weight loss calculated from the TG curve was 82%.
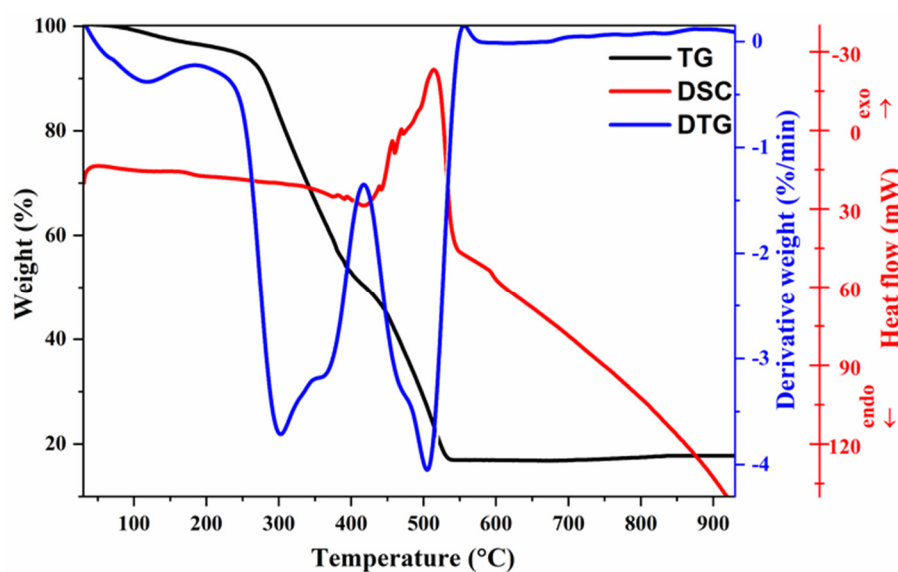

Figure 1. TG-DTG-DSC curves of Sr-Ti-O gel.

For comparison, the thermal decomposition of the gel with the highest BMO content (0.5STO-0.5BMO) was also studied (Figure 2). The degradation behavior is very similar to that of the gel of pristine STO, so it can also be considered a three-step process, and the final weight loss is 80%. The remarkable feature is that the final exothermic degradation step occurs at a slightly lower temperature and the residual mass remains constant at temperatures above approximately 480 °C. This difference can be associated with the enhanced content of nitrate ions, which appear in the gel with appropriate metal precursors, instead of titanium isopropoxide.
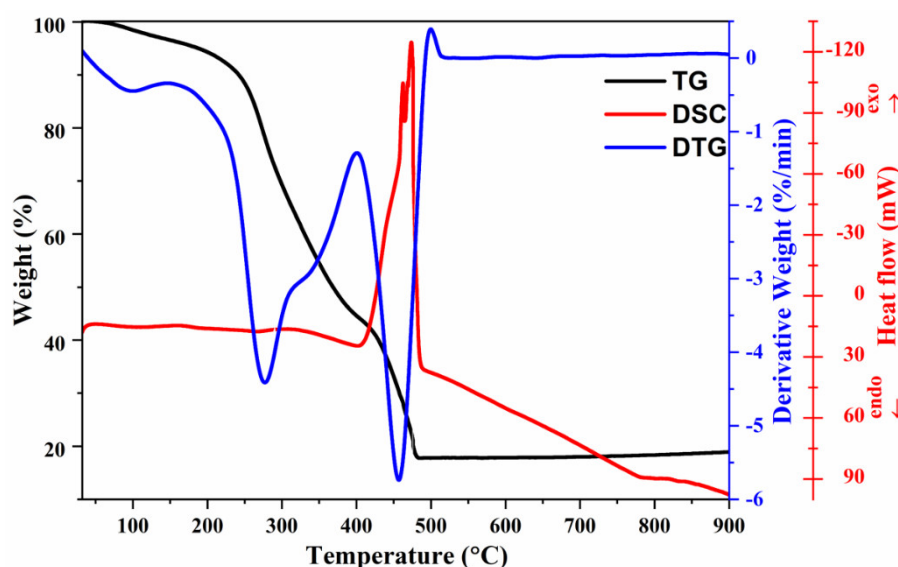

**Figure 2.** TG-DTG-DSC curves of 0.5 (Sr-Ti-O)-0.5 (Bi-Mn-O) gel.

Based on the results of the thermal analysis (TG curve), it can be suggested that the minimal annealing temperature for the formation of the mixed metal oxides is 460 °C. However, XRD analysis revealed that the preparation of (1−x)STO−xBMO solid solutions at such a low temperature was impossible, since the obtained powders were amorphous and at higher temperatures, polyphasic products were formed. Therefore, a 1000 °C temperature was required for the successful synthesis of highly crystalline materials. Figure 3 represents the XRD patterns of STO-BMO solid solutions.

It is evident that after the thermal treatment, the pristine STO sample can be characterized as monophasic perovskite material and no traces of impurity phases can be detected. According to the position and intensity of the reflection peaks, the XRD profile matches standard XRD data of $SrTiO_3$ very well (COD #96-900-6865; space group Pm3m; lattice constant a = 3.90528 Å). By employing Rietveld refinement, the cell parameter a = 3.90341 ± 0.00004 Å was calculated and a cubic structure with the space group Pm3m for the pure STO sample was determined. These results are in good agreement with previously reported studies on thin film [34] and bulk [35] STO. The introduction of BMO into the STO structure did not result in any significant structural changes since there is no visible peak splitting or the appearance of extra peaks associated with anything other than perovskite phase. The samples with a higher BMO content (40 and 50 mol%) have a negligible amount of neighboring Mn_3O_4 phase (COD# 96-151-4241). The amount of secondary phase was determined from Rietveld refinement to be 5 and 6% for 0.6STO-0.4BMO and 0.5STO-0.5BMO samples, respectively. Moreover, there was no considerable change in the peak position, despite the different amount of BMO in solid solutions. Similar results were observed in our previous work, where BMO did not cause any visible change in the XRD patterns when introduced into a $BaTiO_3$ crystal structure [36]. Since Bi^{3+} is smaller than Sr^{2+} (1.17 Å versus 1.26 Å in VIII fold coordination) and Mn^{3+} is larger than Ti^{4+} (0.645 Å versus 0.605 Å in VI fold coordination) [37], it is believed that the mismatch in both A and B site elements compensate each other. The products obtained with a BMO content higher than 50 mol% contained a noticeably higher amount of crystalline impurities.
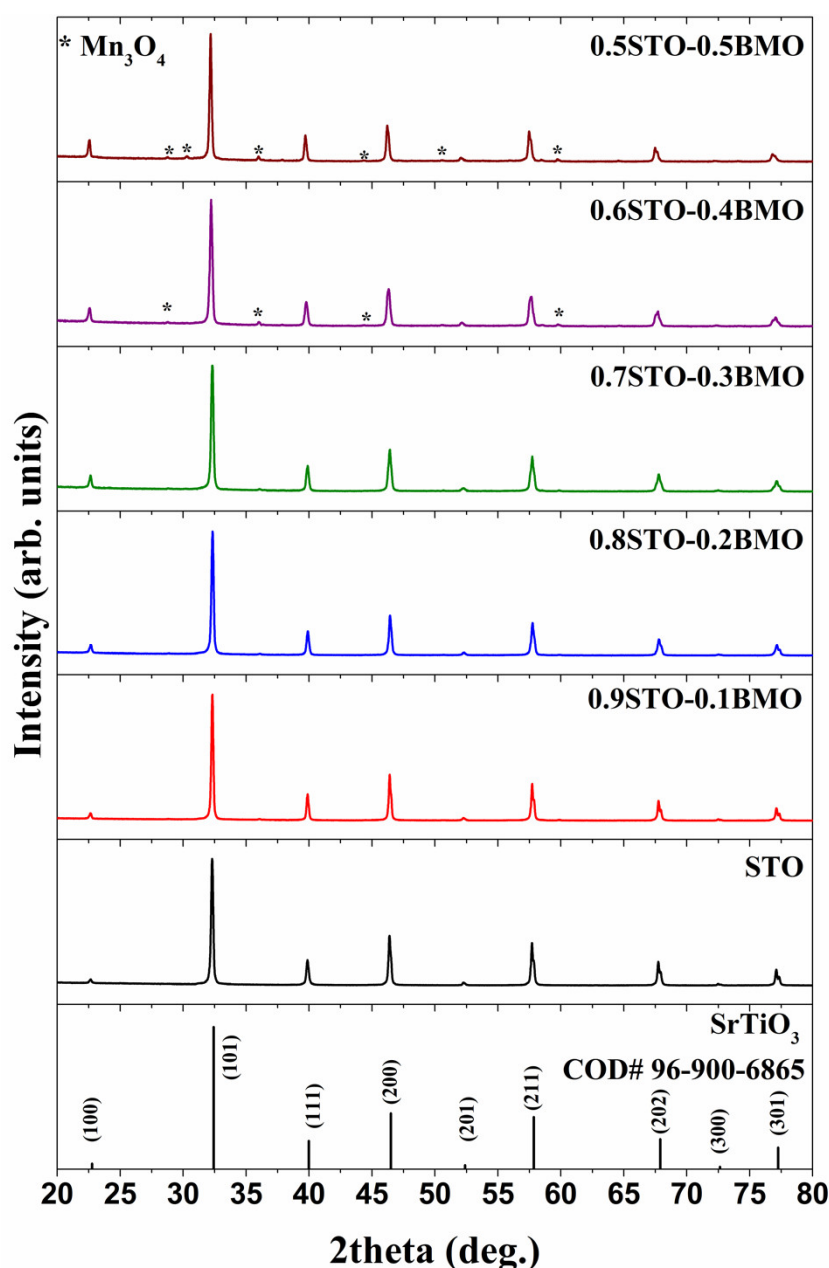
Figure 3. XRD patterns of (1−x)SrTiO₃ (STO)-xBiMnO₃ (BMO) solid solutions annealed at 1000 °C.

For further structural studies, FT-IR spectroscopy was performed for all samples. The FT-IR spectra of (1−x)STO-xBMO solid solutions are represented in Figure 4. It is known that the FT-IR spectral region of 600–100 cm^{-1} contains three types of vibrations for cubic SrTiO₃ perovskite: Ti-O bond stretching vibration at 555 cm^{-1}; Ti-O-Ti bending vibration at 185 cm^{-1}; and Sr-TiO₃ lattice mode at 100 cm^{-1} [38]. For our synthesized pristine STO sample, only one broad peak can be observed at 554 cm^{-1}, which can be attributed to Ti-O stretching vibration. With an increasing amount of BMO, the peak center gradually shifts to higher wavenumbers and reaches 622 cm^{-1} for the 0.5STO-0.5BMO sample. According to previous studies, the FT-IR spectrum of phase-pure BMO has two sharp peaks attributed to Mn-O stretching vibrations at 827 and 722 cm^{-1} [39]. The observed peak shift is the result of the superposition effect of Mn-O and Ti-O bond lengths. In pure STO, Ti^{4+} cations and 6 O^{2-} anions form TiO_6 octahedra. When introducing Mn^{3+} into the perovskite structure instead of Ti^{4+}, Mn^{3+} cations can form MnO_6 octahedra. This substitution causes the changes in the average M-O (where M is Ti^{4+} or Mn^{3+}) distances in the octahedra. Furthermore, there are no absorption peaks belonging to the impurity phase of Mn₃O₄, which should be located at 631, 529, and 416 cm^{-1}, confirming that the amount of this minor phase is negligible [40].
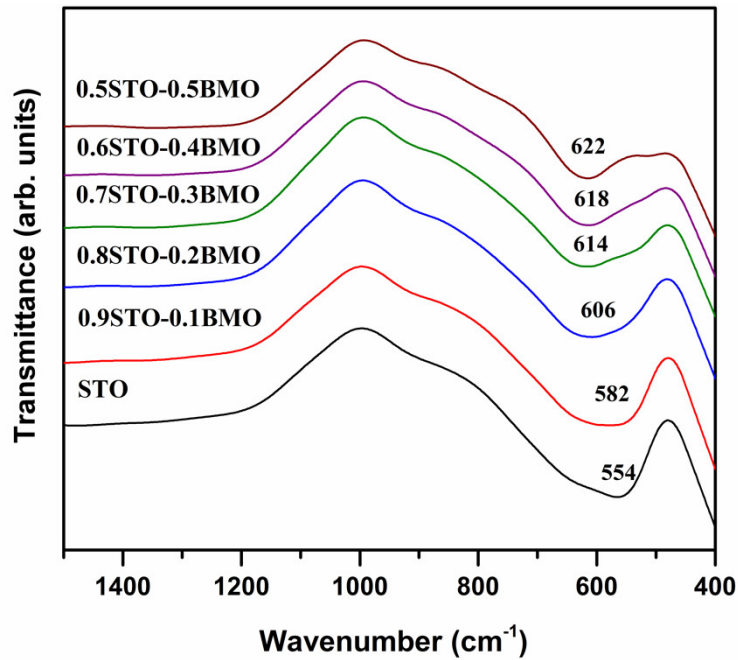
Figure 4. FT-IR spectra of (1−x)STO-xBMO solid solutions annealed at 1000 °C.

The morphology of synthesized (1−x)STO-xBMO solid solutions was examined using SEM. Figure 5 demonstrates the SEM micrographs of STO and representative STO-BMO powders of different compositions. It can be seen that STO powders are composed of mostly uniform and agglomerated nanosized particles, and the size of the particles varies in the range of approximately 40-100 nm. The partial substitution of STO by BMO unequivocally stimulates the significant growth of grains. The sample containing 20 mol% of BMO displays clearly larger particles, and grains with a size of approximately 1–2 μm can be seen. On the other hand, some smaller particles of 0.25–0.6 μm can also be noticed in this sample.
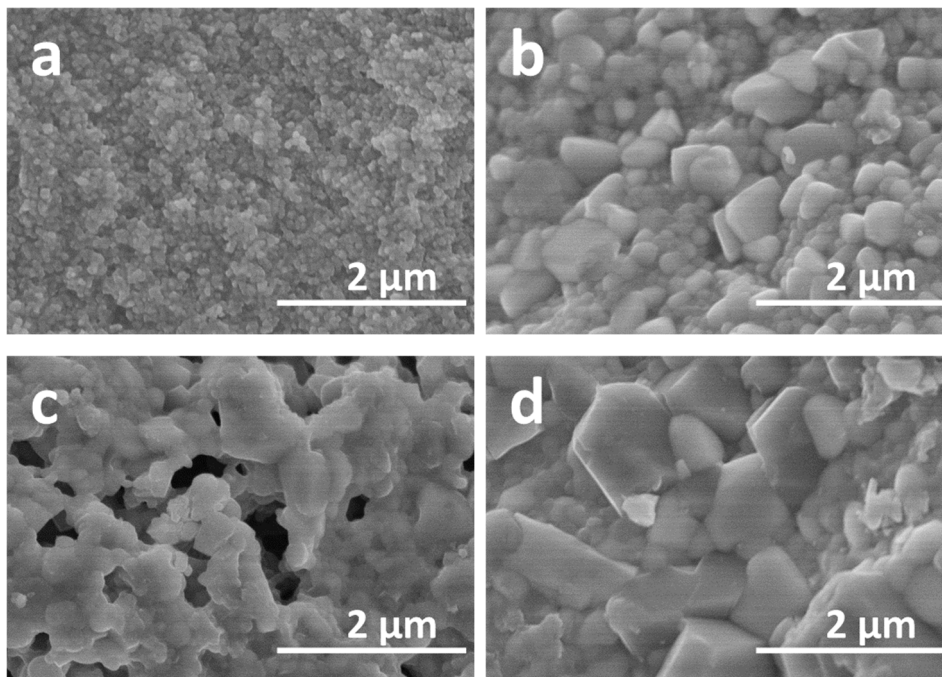
Figure 5. SEM micrographs of STO. (**a**) 0.8STO-0.2BMO, (**b**) 0.6STO-0.4BMO (**c**), and 0.5STO-0.5BMO (**d**) solid solutions annealed at 1000 °C.

A further increase in the percentage of the BMO component to 40 mol% resulted in further growth of the grains to 1.2–3 μm. Finally, the largest grains ranging from 1.4 to 5 μm were observed for the 0.5STO-0.5BMO sample. It is known that impurity phases in comparison with major phases can possess a completely different morphology and can be often observed in the grain boundary region [41]. In our case, for samples with a minor Mn_3O_4 phase (Figure 5c,d), we cannot see the formation of particles with obviously different shapes or sizes.

Dependence of the magnetization on the applied magnetic field strength and chemical composition of the solid solutions was further investigated. Room temperature magnetization curves of all samples are represented in Figure 6.
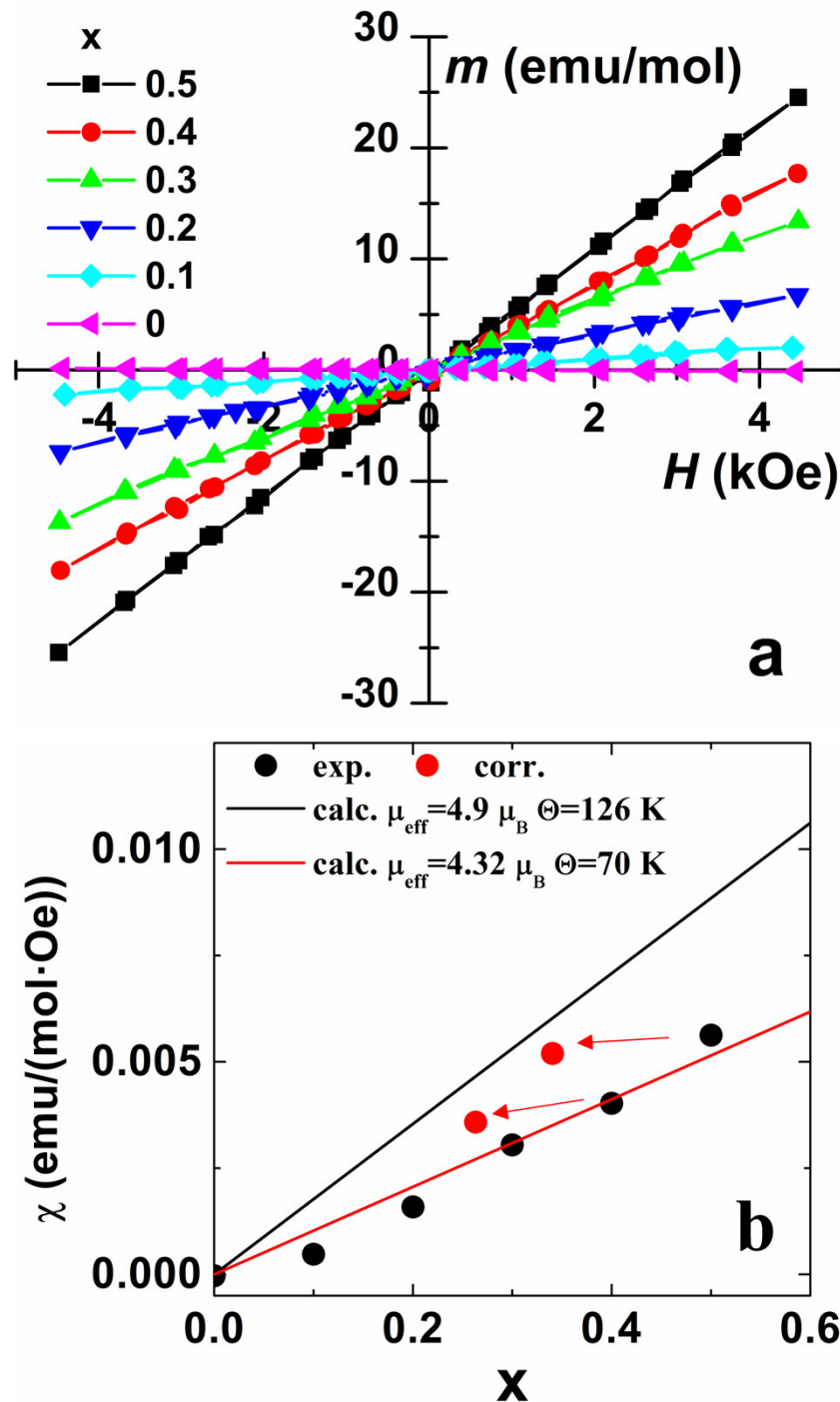
Figure 6. Magnetization curves of (1−x)STO-xBMO solid solutions annealed at 1000 °C (**a**) and a comparison of calculated and experimental molar susceptibility values (**b**).

At room temperature, a pure STO compound is considered to be diamagnetic [42]. Ferromagnetism in pristine STO at room temperature was previously only observed in samples with oxygen-deficiency [43] or by induction with laser annealing [44]. From Figure 6, it can be clearly seen that all BMO-containing samples can be characterized by paramagnetic behavior. For paramagnets, magnetization is proportional to the applied magnetic field m = χH. According to Curie–Weiss law [45,46], the molar susceptibility of samples can be described as follows:

$$\chi = \frac{C}{T - T_c} = \frac{n}{3k_B} \cdot \frac{\mu_{eff}^2}{T - T_c} \tag{1}$$

The inclination of curves (Figure 6a) is defined by BMO molar contribution x, effective magnetic moment of Mn atom μ_{eff}, and Weiss temperature Θ, which depend on the magnetic ordering type and temperature, and thus on the composition and structure of the samples. N_A is the Avogadro number and χ_0 is the small temperature independent term. An increase of the amount of BMO in solid solutions results in a gradual increase in magnetization. On the other hand, the Mn_3O_4 phase is also known to be paramagnetic at room temperature [47,48]. This means that the Mn_3O_4 impurity phase can contribute to the paramagnetism of samples with a higher BMO content (40 and 50 mol%). The data in Figure 6b were compared with the dependences of Equation (1), assuming previously determined values of $\Theta \approx 126$ K and $\mu_{eff} = 4.91\mu_B$ for BMO [46]. The effective magnetic moment $\mu_{eff} = g\sqrt{S(S+1)}\mu_B = 4.9\mu_B$, where the gyromagnetic ratio g = 2 and spin S = 2, is characteristic of Mn^{3+}. However, for BMO nanoparticles, lower values of $\mu_{eff} \leq 4.32\mu_B$ and $\Theta \leq 70$ K were obtained [49]. The smaller effective magnetic moment can be explained by the potential contribution of Mn^{4+}. The Weiss temperature Θ is expected to decrease with a decrease in the amount of BMO in solid solution, as Mn is more diluted, decreasing the exchange interaction strength.

Due to the contribution of Mn_3O_4, the susceptibility and amount of Mn in STO-BMO solutions were corrected. The molar contribution of Mn_3O_4 y = 0.05 and 0.06 for 0.6STO-0.4BMO and 0.5STO-0.5BMO samples, respectively, adds to the total susceptibility of samples, according to $\chi = (1-y)\chi^{STO-BMO} + y\chi^{Mn_3O_4}$, where $\chi^{Mn_3O_4}$ is the susceptibility of Mn_3O_4 [48] and $\chi^{STO-BMO}$ is that of STO-BMO solid solution. The molar contribution of Mn in STO-BMO solid solutions $\chi^{STO-BMO}$ decreases because of the formation of Mn_3O_4 as the amount of Mn in both phases is $\chi = (1-y)\chi^{STO-BMO} + 3y$. The corrected values (red points in Figure 6b) fit the line obtained with $\mu_{eff} = 4.9\mu_B$ for Mn^{3+} in solid solutions relatively well, however, considering that a composition with smaller x should result in a lower Θ.

4. Conclusions

In this work, $(1-x)SrTiO_3-xBiMnO_3$ ($(1-x)STO-xBMO$) solid solutions were synthesized for the first time, employing an aqueous sol-gel method. The single-phase perovskites were obtained in the compositional range of 0 to 30 mol% of BMO. The formation of a negligible amount of neighboring Mn_3O_4 impurity phase was observed for the samples with a higher amount of BMO. FT-IR analysis of synthesized specimens showed gradual spectral change associated with the superposition effect of Mn-O and Ti-O bond lengths with an increase of the BMO content in the solid solutions. The introduction of BMO into STO led to a considerable increase in the grain size. The magnetic properties of the samples were determined to be strongly dependent on the chemical composition of the samples. Paramagnetic behavior was observed for all BMO-containing samples and the magnetization values increased with an increase in the amount of BMO. It was demonstrated that the sol-gel synthetic approach is a suitable method for the successful preparation of $BiMnO_3$-containing mixed metal oxides. This work can be considered as a starting point in the investigation of the structural and physical properties of STO-BMO solid solutions.

References

1. Zavaliche, F.; Zheng, H.; Mohaddes-Ardabili, L.; Yang, S.Y.; Zhan, Q.; Shafer, P.; Reilly, E.; Chopdekar, R.; Jia, Y.; Wright, P.; et al. Electric Field-Induced Magnetization Switching in Epitaxial Columnar Nanostructures. *Nano Lett.* **2005**, *5*, 1793–1796, doi:10.1021/nl051406i.

2. Evans, D.M.; Schilling, A.; Kumar, A.; Sanchez, D.; Ortega, N.; Arredondo, M.; Katiyar, R.S.; Gregg, J.M.; Scott, J.F. Magnetic switching of ferroelectric domains at room temperature in multiferroic PZTFT. *Nat. Commun.* **2013**, *4*, 1534, doi:10.1038/ncomms2548.

3. Leung, C.M.; Sreenivasulu, G.; Zhuang, X.; Tang, X.; Gao, M.; Xu, J.; Li, J.; Zhang, J.; Srinivasan, G.; Viehland, D. A Highly Efficient Self-Biased Nickel-Zinc Ferrite/Metglas/PZT Magnetoelectric Gyrator. *Phys. Status Solidi (RRL)-Rapid Res. Lett.* **2018**, *12*, 1800043, doi:10.1002/pssr.201800043.

4. Marauska, S.; Jahns, R.; Greve, H.; Quandt, E.; Knöchel, R.; Wagner, B. MEMS magnetic field sensor based on magnetoelectric composites. *J. Micromech. Microeng.* **2012**, *22*, 65024, doi:10.1088/0960-1317/22/6/065024.

5. Bur, A.; Wong, K.; Zhao, P.; Lynch, C.S.; Amiri, P.K.; Wang, K.L.; Carman, G.P. Electrical control of reversible and permanent magnetization reorientation for magnetoelectric memory devices. *Appl. Phys. Lett.* **2011**, *98*, 262504, doi:10.1063/1.3605571.

6. Jain, A.; Wang, Y.; Wang, N.; Li, Y.; Wang, F. Emergence of ferrimagnetism along with magnetoelectric coupling in Ba0.83Sr0.07Ca0.10TiO3/BaFe12O19 multiferroic composites. *J. Alloys Compd.* **2020**, *818*, 152838, doi:10.1016/j.jallcom.2019.152838.

7. Jain, A.; Wang, Y.; Wang, N.; Li, Y.; Wang, F. Existence of heterogeneous phases with significant improvement in electrical and magnetoelectric properties of BaFe12O19/BiFeO3 multiferroic ceramic composites. *Ceram. Int.* **2019**, *45*, 22889–22898, doi:10.1016/j.ceramint.2019.07.332.

8. Belik, A.A. Polar and nonpolar phases of BiMO3: A review. *J. Solid State Chem.* **2012**, *195*, 32–40, doi:10.1016/j.jssc.2012.01.025.

9. Jeen, H.; Singh-Bhalla, G.; Mickel, P.R.; Voigt, K.; Morien, C.; Tongay, S.; Hebard, A.F.; Biswas, A. Growth and characterization of multiferroic BiMnO3 thin films. *J. Appl. Phys.* **2011**, *109*, 74104, doi:10.1063/1.3561860.

10. Son, J.Y.; Shin, Y.H. Multiferroic BiMnO3 thin films with double SrTiO3 buffer layers. *Appl. Phys. Lett.* **2008**, *93*, 62902, doi:10.1063/1.2970038.

11. Dos Santos, A.M.; Cheetham, A.K.; Atou, T.; Syono, Y.; Yamaguchi, Y.; Ohoyama, K.; Chiba, H.; Rao, C.N.R. Orbital ordering as the determinant for ferromagnetism in biferroic BiMnO3. *Phys. Rev. B* **2002**, *66*, 064425, doi:10.1103/physrevb.66.064425.

12. De Luca, G.M.; Preziosi, D.; Chiarella, F.; Di Capua, R.; Gariglio, S.; Lettieri, S.; Salluzzo, M. Ferromagnetism and ferroelectricity in epitaxial BiMnO3 ultra-thin films. *Appl. Phys. Lett.* **2013**, *103*, 062902, doi:10.1063/1.4818136.

13. Montanari, E.; Righi, L.; Calestani, G.; Migliori, A.; Gilioli, E.; Bolzoni, F. Room Temperature Polymorphism in Metastable BiMnO3 Prepared by High-Pressure Synthesis. *Chem. Mater.* **2005**, *17*, 1765–1773, doi:10.1021/cm048250s.

14. Toulemonde, P.; Darie, C.; Goujon, C.; Legendre, M.; Mendonça, T.; Álvarez-Murga, M.; Simonet, V.; Bordet, P.; Bouvier, P.; Kreisel, J.; et al. Single crystal growth of BiMnO3 under high pressure–high temperature. *High Press. Res.* **2009**, *29*, 600–604, doi:10.1080/08957950903467050.

15. Muta, H.; Kurosaki, K.; Yamanaka, S. Thermoelectric properties of rare earth doped SrTiO3. *J. Alloys Compd.* **2003**, *350*, 292–295, doi:10.1016/s0925-8388(02)00972-6.

16. Iwashina, K.; Kudo, A. Rh-Doped SrTiO3 Photocatalyst Electrode Showing Cathodic Photocurrent for Water Splitting under Visible-Light Irradiation. *J. Am. Chem. Soc.* **2011**, *133*, 13272–13275, doi:10.1021/ja2050315.

17. Guo, Y.; Kakimoto, K.-I.; Ohsato, H. Dielectric and piezoelectric properties of lead-free $(Na_{0.5}K_{0.5})NbO_3$–$SrTiO_3$ ceramics. *Solid State Commun.* **2004**, *129*, 279–284, doi:10.1016/j.ssc.2003.10.026.

18. Ahadi, K.; Galletti, L.; Li, Y.; Salmani-Rezaie, S.; Wu, W.; Stemmer, S. Enhancing superconductivity in $SrTiO_3$ films with strain. *Sci. Adv.* **2019**, *5*, eaaw0120, doi:10.1126/sciadv.aaw0120.

19. Hui, S.; Petric, A. Evaluation of yttrium-doped SrTiO3 as an anode for solid oxide fuel cells. *J. Eur. Ceram. Soc.* **2002**, *22*, 1673–1681, doi:10.1016/s0955-2219(01)00485-x.

20. Rowley, S.E.; Spalek, L.J.; Smith, R.P.; Dean, M.P.M.; Itoh, M.; Scott, J.F.; Lonzarich, G.G.; Saxena, S.S. Ferroelectric quantum criticality. *Nat. Phys.* **2014**, *10*, 367–372, doi:10.1038/nphys2924.

21. Itoh, M.; Wang, R.; Inaguma, Y.; Yamaguchi, T.; Shan, Y.J.; Nakamura, T. Ferroelectricity Induced by Oxygen Isotope Exchange in Strontium Titanate Perovskite. *Phys. Rev. Lett.* **1999**, *82*, 3540–3543, doi:10.1103/physrevlett.82.3540.

22. Lemanov, V.V.; Smirnova, E.P.; Syrnikov, P.P.; Tarakanov, E.A. Phase transitions and glasslike behavior in $Sr_{1-x}Ba_xTiO_3$. *Phys. Rev. B* **1996**, *54*, 3151–3157, doi:10.1103/PhysRevB.54.3151.

23. Li, X.; Qiu, T.; Zhang, J.; Baldini, E.; Lu, J.; Rappe, A.M.; Nelson, K.A. Terahertz field–induced ferroelectricity in quantum paraelectric $SrTiO_3$. *Science* **2019**, *364*, 1079–1082, doi:10.1126/science.aaw4913.

24. Zhang, S.; Liu, J.; Han, Y.; Chen, B.; Li, X. Formation mechanisms of $SrTiO_3$ nanoparticles under hydrothermal conditions. *Mater. Sci. Eng. B* **2004**, *110*, 11–17, doi:10.1016/j.mseb.2004.01.017.

25. Chen, W.; Liu, H.; Li, X.; Liu, S.; Gao, L.; Mao, L.; Fan, Z.; Shangguan, W.; Fang, W.; Liu, Y. Polymerizable complex synthesis of $SrTiO_3$:(Cr/Ta) photocatalysts to improve photocatalytic water splitting activity under visible light. *Appl. Catal. B Environ.* **2016**, *192*, 145–151, doi:10.1016/j.apcatb.2016.03.057.

26. Silva, E.R.; Curi, M.; Furtado, J.; Ferraz, H.; Secchi, A.R. The effect of calcination atmosphere on structural properties of Y-doped $SrTiO_3$ perovskite anode for SOFC prepared by solid-state reaction. *Ceram. Int.* **2019**, *45*, 9761–9770, doi:10.1016/j.ceramint.2019.02.011.

27. Duong, H.P.; Mashiyama, T.; Kobayashi, M.; Iwase, A.; Kudo, A.; Asakura, Y.; Yin, S.; Kakihana, M.; Kato, H. Z-scheme water splitting by microspherical Rh-doped SrTiO3 photocatalysts prepared by a spray drying method. *Appl. Catal. B Environ.* **2019**, *252*, 222–229, doi:10.1016/j.apcatb.2019.04.009.

28. Liu, Y.; Qian, Q.; Li, J.; Zhu, X.; Zhang, M.; Zhang, T. Photocatalytic Properties of $SrTiO_3$ Nanocubes Synthesized Through Molten Salt Modified Pechini Route. *J. Nanosci. Nanotechnol.* **2016**, *16*, 12321–12325, doi:10.1166/jnn.2016.12979.

29. Shevchuk, Y.A.; Shevchuk, Y.A.; Korchagina, S.K.; Ivanova, V.V. Dielectric and Magnetic Properties of $SrTiO_3$–BiMnO3Solid Solutions. *Inorg. Mater.* **2004**, *40*, 292–294, doi:10.1023/b:inma.0000020531.20385.f4.

30. Salluzzo, M.; Gariglio, S.; Stornaiuolo, D.; Sessi, V.; Rusponi, S.; Piamonteze, C.; De Luca, G.M.; Minola, M.; Marré, D.; Gadaleta, A.; et al. in $BiMnO_3$/$SrTiO_3$ $LaAlO_3$/$SrTiO_3$ Heterostructures. *Phys. Rev. Lett.* **2013**, *111*, 087204, doi:10.1103/physrevlett.111.087204.

31. Lu, L.; Lv, M.; Liu, G.; Xu, X. Photocatalytic hydrogen production over solid solutions between $BiFeO_3$ and $SrTiO_3$. *Appl. Surf. Sci.* **2017**, *391*, 535–541, doi:10.1016/j.apsusc.2016.06.160.

32. Woodward, D.I.; Reaney, I.M. A structural study of ceramics in the $(BiMnO_3)x$–$(PbTiO_3)_{1-x}$ solid solution series. *J. Phys. Condens. Matter* **2004**, *16*, 8823–8834, doi:10.1088/0953-8984/16/49/002.

33. Karoblis, D.; Mazeika, K.; Baltrunas, D.; Lukowiak, A.; Strek, W.; Zarkov, A.; Kareiva, A. Novel synthetic approach to the preparation of single-phase BixLa1−xMnO3+δ solid solutions. *J. Sol-Gel Sci. Technol.* **2019**, *93*, 650–656, doi:10.1007/s10971-019-05098-w.

34. Sharma, D.; Upadhyay, S.; Satsangi, V.R.; Shrivastav, R.; Waghmare, U.V.; Dass, S. Improved Photoelectrochemical Water Splitting Performance of Cu_2O/$SrTiO_3$ Heterojunction Photoelectrode. *J. Phys. Chem. C* **2014**, *118*, 25320–25329, doi:10.1021/jp507039n.

35. Kim, S.; Choi, H.; Lee, M.; Park, J.; Kim, D.; Do, D.; Kim, M.; Song, T.K.; Kim, W. Electrical properties and phase of BaTiO3–SrTiO3 solid solution. *Ceram. Int.* **2013**, *39*, S487–S490, doi:10.1016/j.ceramint.2012.10.119.

36. Karoblis, D.; Zarkov, A.; Mazeika, K.; Baltrunas, D.; Niaura, G.; Beganskiene, A.; Kareiva, A. Sol-gel synthesis, structural, morphological and magnetic properties of BaTiO3–BiMnO3 solid solutions. *Ceram. Int.* **2020**, *46*, 16459–16464, doi:10.1016/j.ceramint.2020.03.209.

37. Shannon, R.D. Revised effective ionic radii and systematic studies of interatomic distances in halides and chalcogenides. *Acta Crystallogr. Sect. A Cryst. Phys. Diffr. Theor. Gen. Crystallogr.* **1976**, *32*, 751–767, doi:10.1107/s0567739476001551.

38. Perry, C.H.; Khanna, B.N.; Rupprecht, G. Infrared Studies of Perovskite Titanates. *Phys. Rev.* **1964**, *135*, A408–A412, doi:10.1103/physrev.135.a408.

39. Bhardwaj, N.; Gaur, A.; Yadav, K. Effect of doping on optical properties in $BiMn_{1-x}(TE)_xO_3$ (where x = 0.0, 0.1 and TE = Cr, Fe, Co, Zn) nanoparticles synthesized by microwave and sol-gel methods. *Appl. Phys. A* **2017**, *123*, 429, doi:10.1007/s00339-017-1042-y.

40. Ocaña, M. Uniform particles of manganese compounds obtained by forced hydrolysis of manganese (II) acetate. *Colloid Polym. Sci.* **2000**, *278*, 443–449, doi:10.1007/s003960050537.

41. Sinusaite, L.; Popov, A.; Antuzevics, A.; Mazeika, K.; Baltrunas, D.; Yang, J.-C.; Horng, J.L.; Shi, S.; Sekino, T.; Ishikawa, K.; et al. Fe and Zn co-substituted beta-tricalcium phosphate (β-TCP): Synthesis, structural, magnetic, mechanical and biological properties. *Mater. Sci. Eng. C* **2020**, *112*, 110918, doi:10.1016/j.msec.2020.110918.

42. Coey, J.M.D.; Venkatesan, M.; Stamenov, P. Surface magnetism of strontium titanate. *J. Phys. Condens. Matter* **2016**, *28*, 485001, doi:10.1088/0953-8984/28/48/485001.

43. Trabelsi, H.; Bejar, M.; Dhahri, E.; Sajieddine, M.; Valente, M.A.; Zaoui, A.; Moez, B. Effect of the oxygen deficiencies creation on the suppression of the diamagnetic behaviour of $SrTiO_3$ compound. *J. Alloys Compd.* **2016**, *680*, 560–564, doi:10.1016/j.jallcom.2016.04.145.

44. Rao, S.S.; Lee, Y.F.; Prater, J.T.; Smirnov, A.I.; Narayan, J. Laser annealing induced ferromagnetism in $SrTiO_3$ single crystal. *Appl. Phys. Lett.* **2014**, *105*, 042403, doi:10.1063/1.4891184.

45. Kittel, C.; McEuen, P. *Introduction to Solid State Physics*; Wiley: Hoboken, NJ, USA, 1996; Volume 8.

46. Belik, A.A.; Takayama-Muromachi, E. Magnetic Properties of $BiMnO_3$ Studied with Dc and Ac Magnetization and Specific Heat. *Inorg. Chem.* **2006**, *45*, 10224–10229, doi:10.1021/ic061400b.

47. Dwight, K.; Menyuk, N. Magnetic Properties of Mn_3O_4 and the Canted Spin Problem. *Phys. Rev.* **1960**, *119*, 1470–1479, doi:10.1103/physrev.119.1470.

48. Srinivasan, G.; Seehra, M.S. Magnetic properties of Mn_3O_4 and a solution of the canted-spin problem. *Phys. Rev. B* **1983**, *28*, 1–7, doi:10.1103/physrevb.28.1.

49. Stanojević, Z.M.; Branković, Z.; Jagličić, Z.; Jagodič, M.; Mančić, L.; Bernik, S.; Rečnik, A. Structural and magnetic properties of nanocrystalline bismuth manganite obtained by mechanochemical synthesis. *J. Nanopart. Res.* **2011**, *13*, 3431–3439, doi:10.1007/s11051-011-0265-7.

Publisher's Note: MDPI stays neutral with regard to jurisdictional claims in published maps and institutional affiliations.